Title

Composite Cathode Design for High-Energy All-Solid-State Lithium Batteries with Long Cycle Life

Journal

ACS Energy Letters, 8(1)

ISSN

2380-8195

Authors

Kim, Young

Cha, Hyungyeon

Kostecki, Robert

et al.

Publication Date

2023-01-13

DOI

10.1021/acsenergylett.2c02414

ACS Energy LETTERS

http://pubs.acs.org/journal/aelccp

Composite Cathode Design for High-Energy All-Solid-State Lithium Batteries with Long Cycle Life

Se Young Kim, Hyungyeon Cha, Robert Kostecki, and Guoying Chen*

Cite This: *ACS Energy Lett.* 2023, 8, 521−528

Read Online

ACCESS | Metrics & More | Article Recommendations | Supporting Information

ABSTRACT: All-solid-state batteries (ASSBs) consisting of a 4 V class layered oxide cathode active material (CAM), an inorganic solid-state electrolyte (SE), and a lithium metal anode are considered the future of energy storage technologies. To date, aside from the known dendrite issues at the anode, cathode instabilities due to oxidative degradation of the SE and reactivities between the SE and CAM as well as loss of mechanical integrity are considered to be the most significant barriers in ASSB development. In the present study, we address these challenges by developing composite cathode structures featuring two key design elements: (1) a halide SE with high oxidative stability to enable direct use of an uncoated 4 V class CAM and (2) a single-crystal (SC) CAM to eliminate intergranular cracking associated with volume changes and mechanical instability. We demonstrate exceptional performance achieved on such ASSB cells incorporating an uncoated SC-$LiNi_{0.8}Co_{0.1}Mn_{0.1}O_2$ (NMC811) CAM, a Li_3YCl_6 (LYC) SE, and a Li−In alloy anode, delivering a high discharge capacity of 170 mAh/g at C/5 and an impressive capacity retention of nearly 90% after 1000 cycles. Through comparative studies on polycrystalline and single-crystal NMC811 composite cathodes, we reveal the working mechanism that enables such stable cycling in the latter cell design. The study highlights the importance of proper cathode composite design and provides key insights in the future development of better-performing ASSB cells.

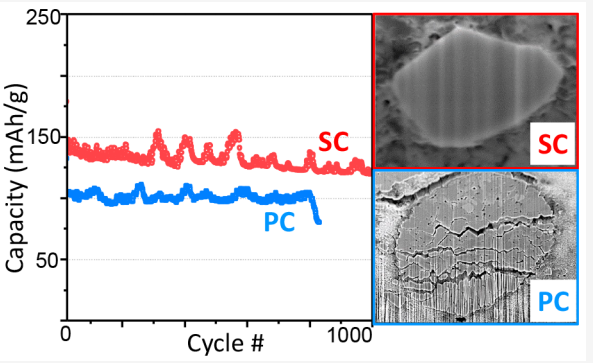

In recent years, the electric vehicle (EV) market has grown rapidly due to the high energy and power densities as well as the long cycle life of lithium-ion batteries (LIBs).[1,2] In order to power future EVs with a longer drive range (≥500 km), further improvements in energy density are being made on traditional LIBs. However, the presence of organic liquid electrolytes brings about fundamental safety issues, as their reactivity and flammability subject the batteries to thermal runaway.[3−6] In this regard, all-solid-state batteries (ASSBs) consisting of a 4 V class cathode active material (CAM), a solid-state electrolyte (SE), and a lithium metal anode are attractive alternatives, as they are poised to deliver higher energy density and better safety performance.[7,8]

Issues associated with dendrite growth at the lithium metal anode are well-known, and they have been investigated for decades in liquid-based LIBs. For ASSB development, aside from the degradation at the anode interface, a number of challenges also arise from the electrochemical and chemo-mechanical instabilities of the SE. For example, oxide materials such as perovskites, garnets, and NASICON-/LiSICON-type superionic conductors have been explored due to their high lithium ion conductivity (∼0.1−1 mS cm^{-1}) and a large electrochemical stability window of up to ∼4.2 V (vs Li^+/Li).[2,9,10] However, the high-temperature sintering process, which is essential for preparing the dense SE separator as well as achieving good contact between the SE and CAM layers, causes chemical degradation and presents challenges in manufacturing and handling.[11] In the case of glass and glass−ceramic types of sulfide SEs, they often have high ionic conductivities of ∼1−10 mS cm^{-1} and excellent ductility, allowing them to establish an intimate contact with CAM.[12,13] However, sulfide SEs suffer from poor electrochemical stability, decomposing at a cathode voltage as low as 2.6 V upon charging.[14] An electronically insulating coating, such as $LiNbO_3$ or $LiNb_{0.5}Ta_{0.5}O_3$, is therefore needed in order to

Received: October 26, 2022
Accepted: December 7, 2022
Published: December 15, 2022

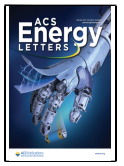

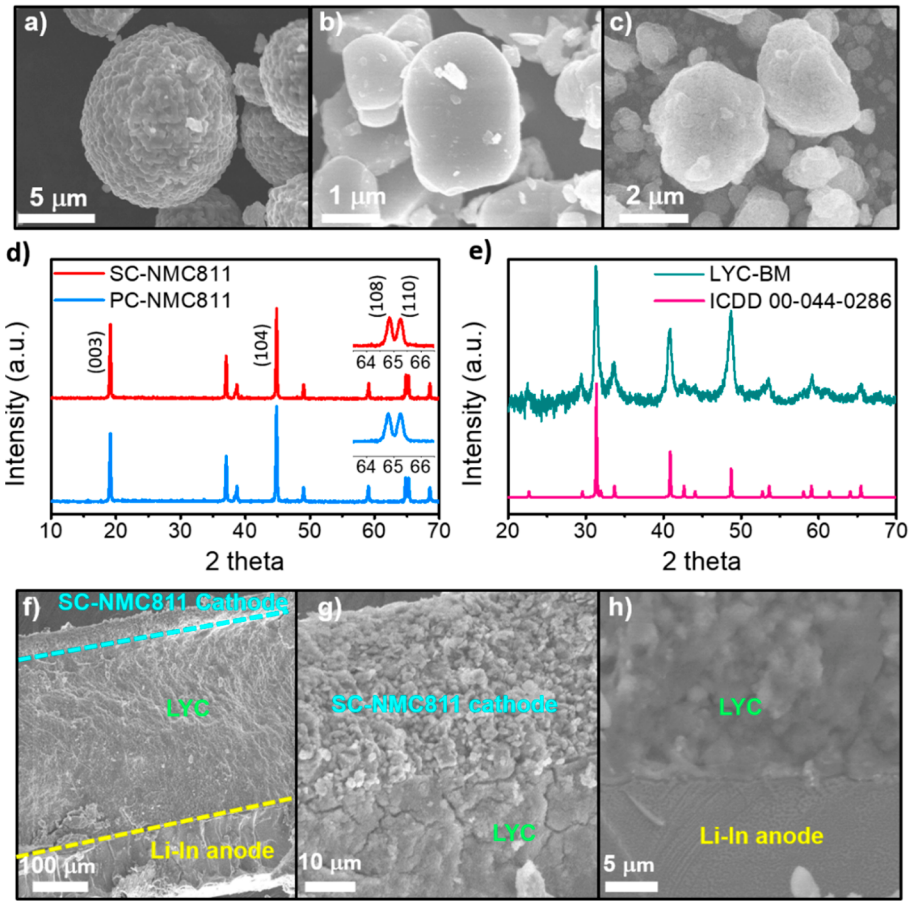

Figure 1. SEM images of pristine powders: (a) PC-NMC811, (b) SC-NMC811, and (c) LYC solid electrolyte. X-ray diffraction patterns of (d) pristine PC-NMC811 and SC-NMC811 and (e) as-prepared LYC SE. ICDD no. 00-044-0286 (space group $P\bar{3}m1$) was added for reference. (f) Cross-sectional SEM images of an as-prepared ASSB cell assembly including a SC-NMC811 composite cathode, an LYC SE, and a Li−In anode. (g, h) Magnified images at the cathode and anode interfaces, respectively.

prevent sulfide SE degradation on the CAM surface.[15,16] Recently, lithium metal halides with the general formula Li_3MCl_6 (M = Sc, In, Y, Er, Yb) were discovered to have a high ionic conductivity (>0.1 mS cm^{-1} at room temperature), a wide electrochemical stability window (up to 4.5 V vs Li^+/Li) and good ductility, allowing them to be used with a 4 V class CAM without a coating.[17−20] In the short period since their introduction, halide solid electrolytes (HSEs) have shown great promise. More recent work by Nazar's group highlights a $Li_2In_{1/3}Sc_{1/3}Cl_4$ HSE with a very high conductivity of 2 mS cm^{-1}. Stable cycling as well as a stable interface between the CAM and HSE were demonstrated on ASSB cells with uncoated $LiCoO_2$ and $LiNi_{0.85}Mn_{0.05}Co_{0.1}O_2$ cathodes.[21]

To further improve ASSB performance, careful design of the composite cathode is needed. Conventional polycrystalline (PC) $LiNi_xMn_yCo_{1-x-y}O_2$ (NMC) materials are large spherical secondary particles made up of sub-micrometer primary grains with random orientations. This causes prolonged Li^+ diffusion pathways and nonuniform Li concentration inside the particles, leading to stress and strain and the eventual internal cracking along the grain boundaries. In liquid cells, the electrolyte permeates into the pores and diffuses along the loose grain boundaries, which enables the utilization of an isolated CAM.[22] In ASSBs, however, cracking and volume changes can lead to void formation, contact loss, impedance rise, and capacity fade.[23] These issues become more severe with increasing Ni content, as the NMC particles experience more stress and strain upon larger anisotropic volume changes. So far, high-Ni NMC (Ni >0.8) ASSB cathodes have typically shown lower capacity retention than that of low-Ni cathodes such as $LiNi_{0.6}Mn_{0.2}Co_{0.2}O_2$.[24] To this end, single-crystal (SC) NMCs are rational alternatives to PC particles, as they eliminate intergranular cracking and allow for particle-level surface optimization for fast Li diffusion.[25−29] Previous reports demonstrated more stable cycling of SC-NMC ASSB cells equipped with a sulfide SE.[23,30−32] Combined with $Li_6PS_5Cl_{0.5}Br_{0.5}$, Li_6PS_5Cl, $Li_{10}GeP_2S_{12}$, $LiNbO_3$, or $LiNb_{0.5}Ti_{0.5}O_3$ coated SC-$LiNi_{0.5}Mn_{0.3}Co_{0.2}O_2$ and SC-$LiNi_{0.88}Co_{0.11}Al_{0.01}O_2$ cathode particles were found to be crack-free after long-term cycling. The cycle life, however, remains poor in these studies due to the low oxidative stability of sulfide SEs and the reactivity between the NMC and SE at the interface.[14,23,31,33−35]

Herein, we combine an HSE solid electrolyte with a single-crystal CAM in our composite cathode design to take advantage of the oxidative stability of the HSE and the mechanical stability of SC particles. The concept is demonstrated on ASSB cells with an SC-$LiNi_{0.8}Co_{0.1}Mn_{0.1}O_2$ (NMC811) CAM, an LYC SE, and a Li−In alloy anode. High discharge capacities of 170 mAh/g at 0.2 C and 140 mAh/g at 0.5 C were achieved, along with an excellent discharge capacity retention of ∼90% after 1000 cycles. The SC cell significantly

https://doi.org/10.1021/acsenergylett.2c02414
ACS Energy Lett. 2023, 8, 521−528

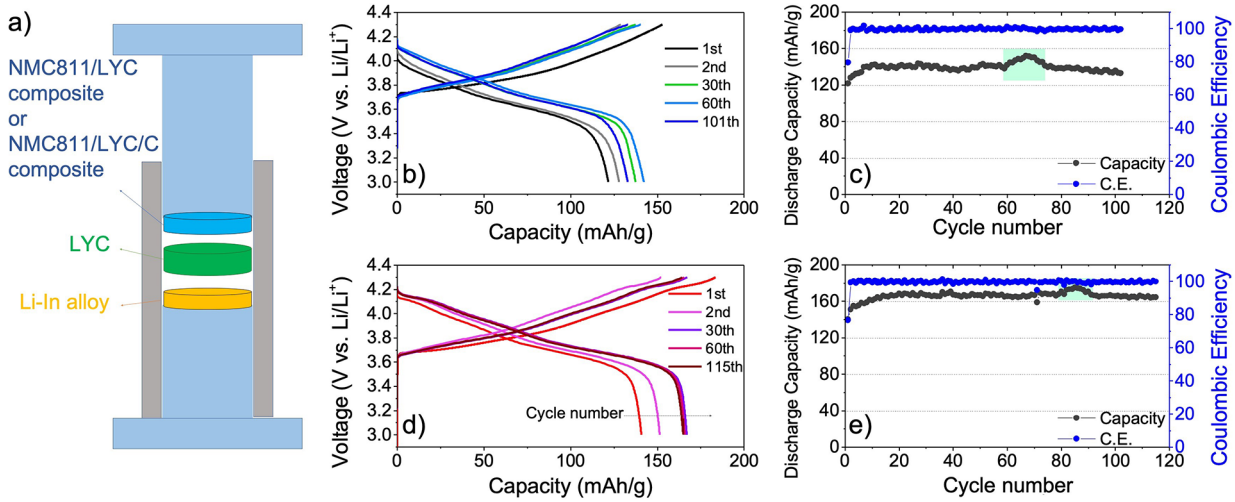

Figure 2. (a) Schematics of ASSB cell configuration. (b–e) SC-NMC811 ASSB cell performance with and without carbon additive in the composite cathode: (b, d) charge/discharge voltage profiles and (c, e) discharge capacity retention and Coulombic efficiency. (b, c) Collected from the cell without carbon. (d, e) Collected from the cell with 2.5 wt % carbon. Green shaded regions in (c) and (e) mark performance fluctuation due to changes in laboratory ambient temperature during the test.

outperforms an equivalent cell with a PC-NMC811 CAM in both kinetics and cycle life. We further compare the degradation mechanisms of PC- and SC-NMC811 cells by using post-mortem scanning electron microscope (SEM) imaging and electrochemical impedance spectroscopy (EIS) analyses, which reveal the detrimental effect of particle cracking in the former while good mechanical integrity and intimate contact between the CAM and SE particles were enabled in the latter.

Material Synthesis and ASSB Cell Configuration. Figure 1a,b shows the SEM images of as-obtained commercial PC-NMC811 and SC-NMC811 particles used for the ASSB cells. While PC-NMC811 shows spherical-shaped secondary particles (8–10 μm) consisting of ~0.5 μm sized primary grains (Figure 1a), the SC-NMC811 sample is composed of 3–5 μm sized primary particles without a defined particle shape (Figure 1b). The collected powder XRD patterns from the PC- and SC-NMC811 samples show that both samples are well crystallized in the layered crystal structure ($R\bar{3}m$) with a d spacing of ~4.62 Å, evidenced by the clear peak splitting of the (110) and (108) reflections in a similar intensity ratio (Figure 1d). Figure 1c shows the SEM image of as-prepared LYC particles synthesized by a high-energy ball-milling method. Due to the nature of the ball-milling process, the particles exhibit various shapes and sizes. The XRD pattern collected on the LYC powder confirms the hexagonal-close-packed (hcp) crystal structure ($P\bar{3}m1$) with a relatively low crystallinity (Figure 1e).[17,23] The measured ionic conductivity of the sample is ~0.32 mS cm^{-1} (Figure S1a), which is consistent with the previous reports on cation-disordered LYC prepared by a similar ball-milling process.[36]

ASSB cells were assembled by using a layer-by-layer approach. LYC was first pelletized under an external pressure of ~100 MPa. The resulting pellets achieved a high density of ~85%, which is similar to what was obtained on other soft SEs such as sulfides,[37−40] confirming the excellent mechanical properties of the HSE. Cathode mixtures containing NMC811 and LYC powders were then pelletized on top of the prepared LYC pellet. Anode fabrication follows a procedure previously reported in the literature,[20] where a In metal disk was first placed onto the LYC pellet before placing the Li metal disk. This allows intimate contact between LYC and In metal after pressing the cell, providing high Li ion diffusivity without a direct contact between LYC and Li metal, which has been shown to induce LYC reduction.[20,41,42] Li and In subsequently form a Li–In alloy (3:7 molar ratio) anode upon cell cycling.[43] Figure 1f–h shows the cross-sectional SEM images of the as-assembled ASSB cell with an SC-NMC811 composite cathode and a Li–In anode. Intimate contact with the LYC SE layer was achieved, at both the densified SC-NMC811 composite cathode side and the metallic anode side.

Electrochemical Performance of the ASSB Cells. Figure 2a shows the schematics of the cell configuration used for electrochemical evaluation at room temperature. A constant pressure of ~8 MPa (1160 psi) was applied externally during all cell testing, similar to the conditions used for other ASSB cells utilizing a soft SE such as a sulfide. We first evaluate the effect of conductive carbon additives by comparing the performance of SC-NMC811 cells with and without 2.5 wt % carbon black added to the composite cathode, which has SC-NMC811/LYC/C weight ratios of 57/40.5/2.5 and 60/40/0, respectively. The SC-NMC811/LYC ratios in both composites were kept similar for comparison purposes. Due to the electronically insulating nature of LYC, negligible capacity was obtained from the cell with the 60/40/0 composite (Figure S1b). The result is consistent with previous reports on the poor performance of cathode composites when a high fraction of halide SE was introduced.[18] Upon reducing the LYC content, improved performance was obtained on a cell with a SC-NMC811/LYC/C ratio of 80/20/0. Figure 2b,c and Figure 2d,e show the electrochemical performance of cathodes with ratios of 57/40.5/2.5 and 80/20/0, respectively. Both cells experienced a capacity increase during initial cycling, indicating a "break-in" process where solid-state conduction pathways are being established. In the presence of carbon, the cell delivered a discharge capacity of ~170 mAh/g after 100 cycles at a C/5 rate, similar to what was reported for an equivalent cell using a liquid electrolyte.[26,27] On the other hand, the cell without carbon only delivered ~140 mAh/g after 100 cycles, about an 18% reduction in capacity. The presence of carbon also

https://doi.org/10.1021/acsenergylett.2c02414
ACS Energy Lett. 2023, 8, 521−528

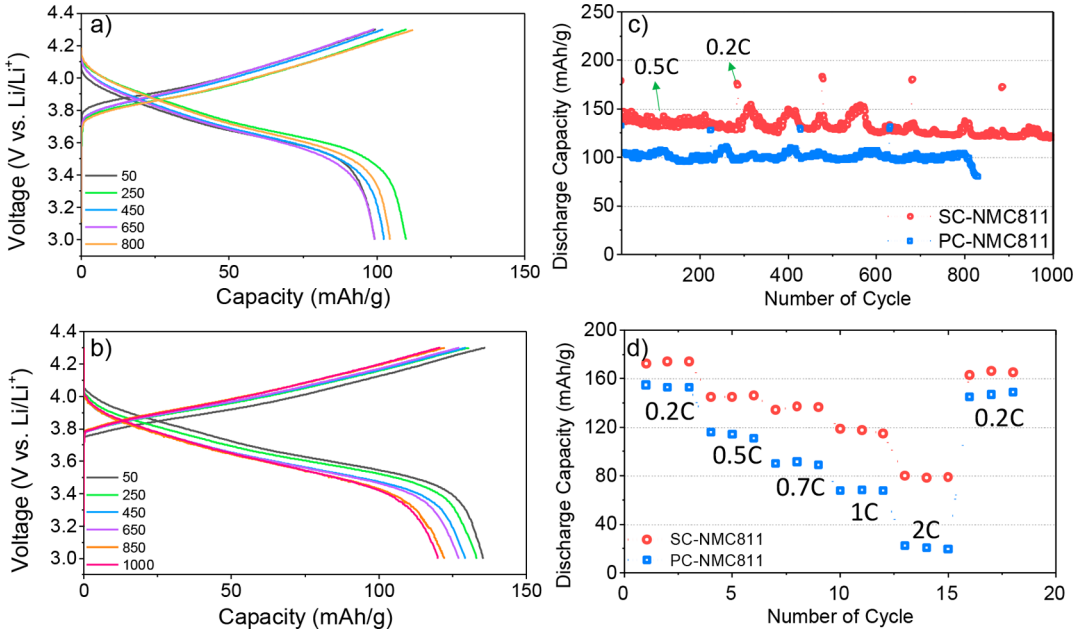

Figure 3. Charge/discharge voltage profiles of (a) PC-NMC811 and (b) SC-NMC811 ASSB cells. (c) Capacity retention plots for the cells cycled at 0.5 C for 200 cycles followed by 3 cycles at 0.2 C. The same sequence repeats throughout the test. Note that the performance fluctuation is due to changes in laboratory ambient temperature during the test. (d) Rate capability comparison of PC-NMC811 and SC-NMC811 ASSB cells.

improves capacity retention, achieving ~117% and 107% after 100 cycles for the cells with and without carbon, respectively. It is worth noting that in sulfide SE based composite cathodes, adding carbon additives has also been shown to compensate for the low electric conductivity and improve initial capacity. However, the presence of carbon deteriorates long-term cycling performance, as it induces SE decomposition at the carbon/SE interface.[44,45] With the high oxidation stability of HSEs, carbon provides a crucial role in facilitating electronic conduction within the cathode composite without the negative impact on SE decomposition, clearly demonstrating the unique advantage of halide SEs in ASSB cells.

For a performance comparison of PC- and SC-NMC cells, we prepared PC-NMC811/LYC/carbon and SC-NMC811/LYC/carbon cathode composites with the same ratio of 57/40.5/2.5. The SEM images of the composites are shown in Figure S2a,d, respectively. The corresponding energy dispersive X-ray spectroscopy (EDX) maps (Figure S2b,c,e,f) suggest that, even in the presence of a carbon additive, the uniform distribution of LYC and NMC811 particles can be achieved in both cases. Figure 3 compares the long-term cell cycling performance carried out by galvanostatic charge and discharge in the voltage window of 3−4.3 V (vs Li^+/Li). The cells were cycled at room temperature at C/2 for 200 cycles and followed by 3 cycles at C/5. This sequence was repeated throughout the testing. PC- and SC-NMC811 cells both display the typical voltage profiles of NMC811 (Figure 3a,b), with slightly lower polarization observed in the SC-NMC811 cell, suggesting improved Li ion diffusion pathways in the latter. Significantly improved cycling performance was observed in the SC-NMC811 cell. At the C/2 rate, the initial discharge capacities were ~105 and 140 mAh/g for PC- and SC-NMC811 cells, respectively, which decreased to ~80 mAh/g after 830 cycles and ~125 mAh/g after 1000 cycles. This corresponds to capacity retentions of ~76% and 89%, respectively (Figure 3c). It is worth noting that the PC-NMC811 cell experienced a rapid capacity decay after ~805 cycles, likely a result of catastrophic failure in one or more components in the cell.

We wish to point out that the SC-NMC811 cell performance represents one of the best reported for ASSBs using a Ni-rich NMC CAM so far. The long-term cycling stability even surpasses that of previous studies carried out using a $LiNbO_3$-coated NMC811 or Li_2O−ZrO_2-coated $LiNi_{0.90}Co_{0.05}Mn_{0.05}O_2$ cathode and a sulfide SE with a high ionic conductivity of ~3 mS cm^{-1}, which is 1 order of magnitude higher than that of LYC (0.32 mS cm^{-1}). In these studies, a lower capacity retention of ~84% at room temperature[20] and ~88% at an elevated temperature of 60 °C were achieved after 1000 cycles.[40] As shown recently by Nazar's group, the SE conductivity plays a significant role in cell performance. By using a highly conductive $Li_2In_xSc_{0.666-x}Cl_4$ SE, ~80% capacity retention can be achieved even after 3000 cycles of a $LiNi_{0.85}Mn_{0.05}Co_{0.1}O_2$ CAM cell.[21] We believe that, coupled with a halide SE more conductive than LYC, our SC-NMC composite cathode design is likely to lead to further advancement in ASSB performance. We are currently investigating similar studies using halide SEs with a higher ionic conductivity.

A rate capability comparison of the PC- and SC-NMC811 cells is shown in Figure 3d, evaluated by gradually increasing the charge and discharge rates from 0.2 C to 0.5 C, 0.7 C, 1 C, and 2C, followed by 0.2 C cycling. The rate capability tests were carried out after 20 cycles at 0.2 C. Compared to the equivalent liquid cells, both ASSB cells showed relatively poor kinetics, consistent with the previous reports on more resistive Li transport in the solid state without any liquid presence. However, the SC-NMC811 cell consistently outperformed the PC counterpart at every rate evaluated, suggesting kinetic enhancement in the SC cell design. This is likely due to the absence of grain boundaries in the SC particles. Although the grain size of SC-NMC811 is larger than that of the primary

https://doi.org/10.1021/acsenergylett.2c02414
ACS Energy Lett. 2023, 8, 521−528

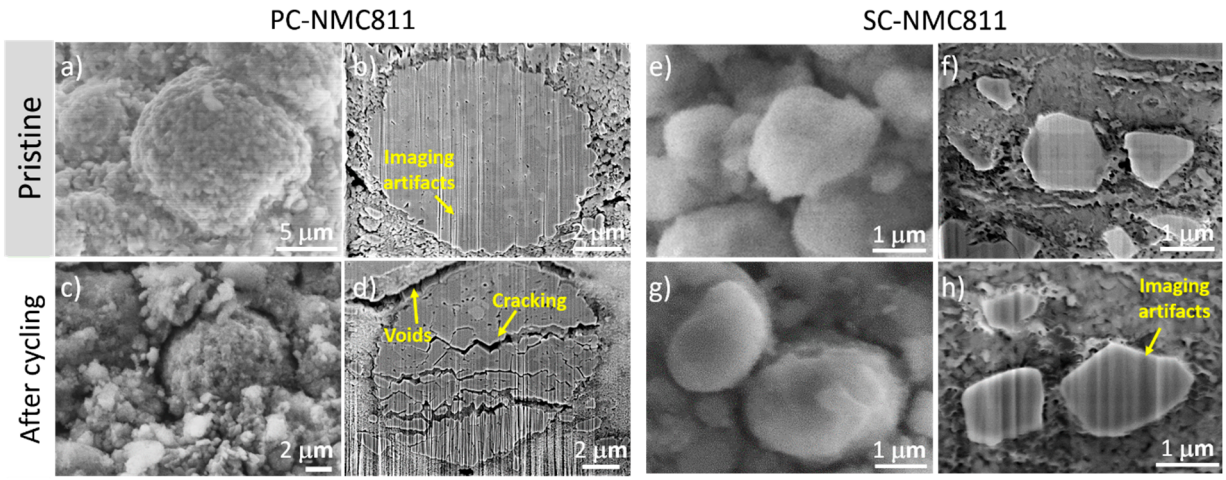

Figure 4. SEM images (a, c, e, g) and cross-sectional FIB-SEM images (b, d, f, h) collected from as-prepared (a, b, e, f) and cycled (c, d, g, h) NMC811 composite cathodes. (a–d) Collected from the PC-NMC811 cell (e, f) cCollected from the SC-NMC811 cell. The vertical lines in (b, d, f, h) are imaging artifacts from FIB processing.

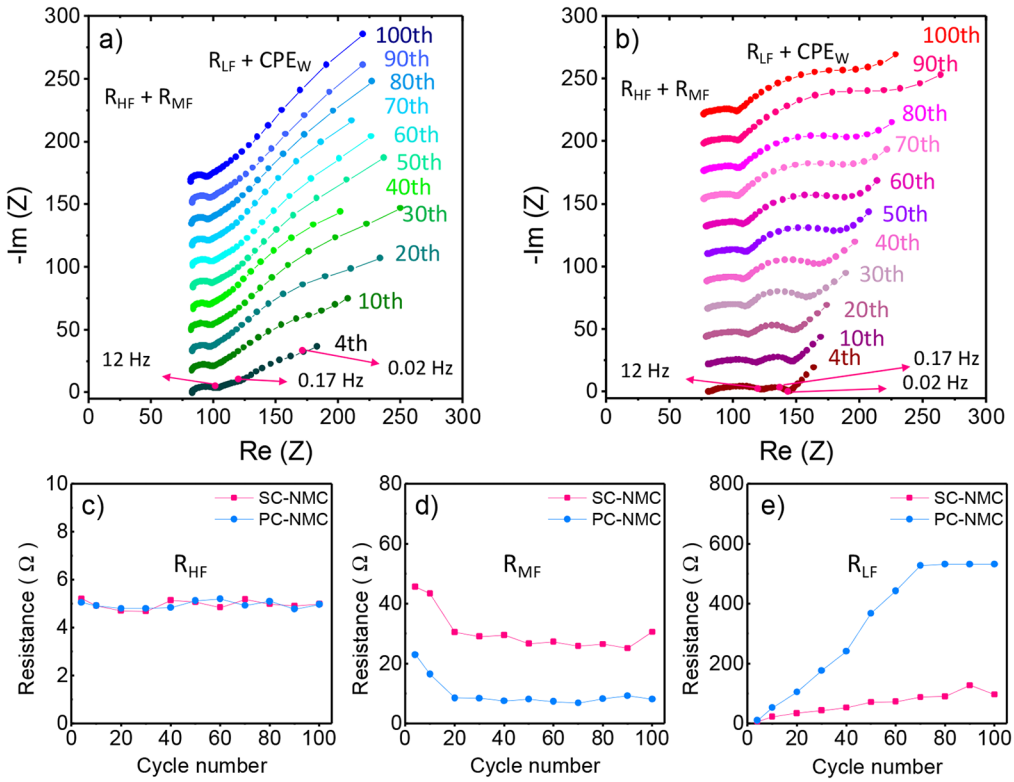

Figure 5. Nyquist plots obtained at 3.67 V during the discharge of (a) PC-NMC811 and (b) SC-NMC811 ASSB cells at the indicated cycle number. (c–e) Resistance values obtained from fitting the corresponding Nyquist plots in (a) and (b). R_{HF} represents impedance from SE grain boundaries, R_{MF} represents impedance from the CAM and SE interface, and R_{LF} includes impedance contributions from the Li–In anode and SE interface as well as Li^+ diffusion within the CAM particles.

particles in PC-NMC811, the presence of grain boundaries in the latter can prolong Li^+ diffusion pathways and lead to more torturous and resistive Li^+ movement in general. The mismatch in grain orientation at the boundaries can also add additional barriers to Li^+ transport.

Understanding the Superior Performance of the SC Cell. A post-mortem analysis was carried out to further understand performance differences observed in PC- and SC-NMC811 ASSB cells. Figure 4 compares morphological changes before and after the long-term cycling of the PC and SC composite cathodes, carried out by using both top-view SEM and cross-sectional view FIB-SEM imaging. While pristine PC-NMC811 consists of dense agglomerates of primary particles (~500 nm size) free of cracking (Figure 4a,b), numerous internal cracks with various sizes and lengths are clearly shown within the secondary particle after 830 cycles (Figure 4c,d). In contrast to the intimate contact observed between the CAM and LYC SE particles, large gaps are visible after cycling, leading to contact loss and discontinuation in Li^+ ion diffusion pathways. These changes are somewhat expected

https://doi.org/10.1021/acsenergylett.2c02414
ACS Energy Lett. 2023, 8, 521–528

due to the known anisotropic volume changes experienced by PC-NMC811 particles during cycling.[28,46] In contrast, both SEM and FIB-SEM images show crack-free SC-NMC811 particles before (Figure 4e,f) and after long-term cycling of 1000 cycles (Figure 4g,h). The contact between the SC-NMC811 and LYC SE particles remains nearly unchanged, enabling efficient Li^+ ion migration during extensive cycling. Further morphological evaluation of the samples is shown in Figure S3. Compared to the pristine PC-NMC811 composite (Figure S3a), several observations can be made on the recovered cathode after 830 cycles, including contact loss between PC-NMC811 and LYC SE particles, internal cracking within the PC-NMC811 secondary particles, and loss of connections in Li^+ pathways, as well as the presence of isolated and inaccessible PC-NMC811 primary particles (Figure S3b–d). On the other hand, no discernible changes were observed by comparing the pristine and cycled SC-NMC811 composites (Figure S3e–h). The SC-NMC811 particles show the absence of cracking and the composite cathode maintains its integrity even after 1000 cycles. The two scenarios provide a marked contrast in terms of the effect of cycling, with the former suffering significant loss of active materials due to isolation and inaccessibility, while the latter maintains high CAM utilization. The results are consistent with the cycling performance differences observed on the two ASSB cells.

To gain further insights into cycling-induced changes in the cell components and at the interfaces, electrochemical impedance spectroscopy was carried out on cells after cycling at 0.2 C for 100 cycles. Consistent with the previous results, the PC-NMC811 cell experienced a gradual capacity decay (Figure S4a) while the SC-NMC811 cell showed a more stable capacity retention (Figure S4b). Figure 5a,b shows the Nyquist plots obtained at open circuit voltage (OCV) after 2 h relaxation following discharging the cell to 3.67 V, with the data plotted at the fourth cycle as well as every tenth cycle. The particular voltage of 3.67 V was chosen due to the known high diffusion coefficient at the corresponding state of charge of NMC811, allowing better differentiation of the impedance components in the ASSB cell.[46,47] In both cases, the typical semicircle shape along with the Warburg element appear in the examined frequency region (1 MHz to 1 mHz). According to previous reports,[48] the bulk SE resistance from the separator layer (R_{SE}) appears at a very high frequency region of >1 MHz while the charge transfer resistance within the grain boundaries of SE evolves in the frequency region of 1 MHz to 1 kHz (R_{HF}). The semicircle appearing in the mid-frequency region of 1 kHz to 10 Hz (R_{MF}) can be attributed to the charge transfer resistance at the interface between NMC811 CAM and LYC SE. In addition, the semicircles at the low-frequency region of <10 Hz (R_{LF}) can be assigned to the interfacial resistance between the LYC SE layer and the In–Li alloy anode as well as Li^+ ion diffusion impedance within the CAM. The latter component is also reflected in the subsequent Warburg region (CPE_W). The assigned impedance component on the Nyquist plots collected at 3.67 V from the fourth discharge are shown in Figure S5. In the Nyquist plots from both cells, the R_{SE} resistance of the LYC SE separator layer was determined to be ∼80 Ω, corresponding to an electrolyte layer thickness of approximately 350 μm and an ionic conductivity of 0.3 mS cm^{-1} in LYC. The R_{SE} values stay more or less constant throughout the cycling. The grain boundary resistance (R_{HF}) of the LYC electrolyte evolves similarly in the frequency range of 0.15 MHz to 5.6 kHz. The R_{MF} component between 5.6 kHz and 12.3 Hz appears to be smaller in the PC cell, and the differences are likely a result of the initial contact made between the CAM and the SE. While the PC particles are largely spherical (Figure 1a) and better for making surface contact, the SC particles are irregularly shaped (Figure 1b). Furthermore, the measured Brunauer–Emmett–Teller (BET) surface areas of the PC-NMC811 and SC-NMC811 samples are 0.64 and 0.27 m^2/g, respectively, suggesting that more surface contact area is available for SE connection in the former. Regardless of the initial R_{MF} size, both cells showed a gradual size reduction over the first 20 cycles or so (Figure 5a,b), indicating a "break-in" process that establishes effective Li^+ ion migration pathways between NMC811 particles and LYC SE. This facilitates Li^+ ion migration upon initial cycling, which is reflected by the small capacity increase in both cells (Figure S4). The R_{MF} component remained more or less constant in the subsequent cycles. The main differences between the two cells are observed in the R_{LF} and CPE_W region below 12 Hz, which includes an impedance contribution from the SE and Li–In anode interface (12.3–0.17 Hz) as well as Li^+ diffusion within the CAM particles (<0.17 Hz). As shown in Figure 5a,b, this component in both cells increases with cycling; however, the extent is significantly more severe in the PC cell. Further analysis was carried out by fitting the EIS data using the equivalent circuit shown in Figure S5c, and the results are given in Table S1 and plotted in Figure 5c–e. The initial R_{LF} values of ∼7–10 Ω are similar, consistent with the pristine materials' properties before cell cycling. Cycling leads to a continuous increase in R_{LF} in both cells. After 100 cycles, a large increase of over 60× was observed in the PC cell, whereas in the SC cell a much smaller increase of ∼10× was observed. Although the impedance evolution at the interface between the LYC SE and Li–In anode also contributes to the increase in the R_{LF} component, it is expected that both cells experience similar changes at the anode interface, as the same configuration was used for the study and the depth of discharge was carefully controlled during the experiment. Li^+ diffusion resistance within NMC811 CAM particles, therefore, is considered to be the main contributor to the observed differences in the R_{LF} and CPE_W components. The observation of lower Li^+ diffusion resistance increase upon cycling of the SC-NMC811 composite is supported by the SEM analysis, demonstrating the unique advantage of using SC particles that provide improved Li^+ ion diffusion pathways due to their better mechanical properties for continuous cycling.

The performance and degradation mechanism of novel ASSB composite cathodes combining an LYC SE and an uncoated NMC811 CAM were investigated. Carbon was found to be beneficial in improving electronic conduction and material utilization without deteriorating LYC, a unique advantage of the halide SEs due to their high oxidative stability. Excellent performance was achieved on a composite design combining LYC SE with SC-NMC811, delivering a capacity retention of nearly 90% after 1000 cycles at a C/2 rate. Through post-mortem diagnostic studies, we show that the superior mechanical stability of SC-NMC811 not only prevents the cathode active particles from cracking but also enables better contact maintenance between the NMC811 CAM and LYC SE during cell cycling. This is in stark contrast to the equivalent cell equipped with PC-NMC811, which experienced significant morphology changes at the cathode, including intergranular cracking of CAM and disconnection

https://doi.org/10.1021/acsenergylett.2c02414
ACS Energy Lett. 2023, 8, 521–528

between the LYC and PC-NMC811 particles. The result is inferior performance in discharge capacity and cycle life as well as the rate capacity of the PC cell. Our study highlights the importance of proper cathode composite design in order to develop high-energy all-solid-state lithium batteries with long cycle life.

■ ASSOCIATED CONTENT

Supporting Information

The Supporting Information is available free of charge at https://pubs.acs.org/doi/10.1021/acsenergylett.2c02414.

Experimental methods, Nyquist plots, SEM images, electrochemical cycling data, equivalent model for EIS data fitting, and resistance values from EIS data fitting (PDF)

■ AUTHOR INFORMATION

Corresponding Author

Guoying Chen − *Energy Storage and Distributed Resources Division, Lawrence Berkeley National Laboratory, Berkeley, California 94720, United States;* orcid.org/0000-0002-3218-2609; Email: gchen@lbl.gov

Authors

Se Young Kim − *Energy Storage and Distributed Resources Division, Lawrence Berkeley National Laboratory, Berkeley, California 94720, United States*

Hyungyeon Cha − *Energy Storage and Distributed Resources Division, Lawrence Berkeley National Laboratory, Berkeley, California 94720, United States*

Robert Kostecki − *Energy Storage and Distributed Resources Division, Lawrence Berkeley National Laboratory, Berkeley, California 94720, United States*

Complete contact information is available at: https://pubs.acs.org/10.1021/acsenergylett.2c02414

Notes

The authors declare no competing financial interest.

■ ACKNOWLEDGMENTS

The authors thank Drs. Yanbao Fu and Vincent Battaglia at Lawrence Berkeley National Laboratory for helping with the BET surface area measurements. Work at the Molecular Foundry was supported by the Office of Science, Office of Basic Energy Sciences, of the U.S. Department of Energy under Contract No. DE-AC02-05CH11231. This work was supported by the Assistant Secretary for Energy Efficiency and Renewable Energy, Office of Vehicle Technologies, of the U.S. Department of Energy under Contract No. DE-AC02-05CH11231.

■ REFERENCES

(1) Manthiram, A. A reflection on lithium-ion battery cathode chemistry. *Nat. Commun.* **2020**, *11*, 1−9.

(2) Turcheniuk, K.; Bondarev, D.; Singhal, V.; Yushin, G. Ten years left to redesign lithium-ion batteries. *Nature* **2018**, *559*, 467−470.

(3) Arbizzani, C.; Gabrielli, G.; Mastragostino, M. Thermal stability and flammability of electrolytes for lithium-ion batteries. *J. Power Sources* **2011**, *196*, 4801−4805.

(4) Murmann, P.; Schmitz, R.; Nowak, S.; Ignatiev, N.; Sartori, P.; Cekic-Laskovic, I.; Winter, M. Electrochemical performance and thermal stability studies of two lithium sulfonyl methide salts in lithium-ion battery electrolytes. *J. Electrochem. Soc.* **2015**, *162*, A1738.

(5) Cao, X.; Ren, X.; Zou, L.; Engelhard, M. H.; Huang, W.; Wang, H.; Matthews, B. E.; Lee, H.; Niu, C.; Arey, B. W.; et al. Monolithic solid−electrolyte interphases formed in fluorinated orthoformate-based electrolytes minimize Li depletion and pulverization. *Nat. Energy* **2019**, *4*, 796−805.

(6) Fan, X.; Chen, L.; Borodin, O.; Ji, X.; Chen, J.; Hou, S.; Deng, T.; Zheng, J.; Yang, C.; Liou, S.-C.; et al. Non-flammable electrolyte enables Li-metal batteries with aggressive cathode chemistries. *Nat. Nanotechnol* **2018**, *13*, 715−722.

(7) Janek, J.; Zeier, W. G. A solid future for battery development. *Nat. Energy* **2016**, *1* (9), 1−4.

(8) Famprikis, T.; Canepa, P.; Dawson, J. A.; Islam, M. S.; Masquelier, C. Fundamentals of inorganic solid-state electrolytes for batteries. *Nat. materials* **2019**, *18*, 1278−1291.

(9) Han, F.; Zhu, Y.; He, X.; Mo, Y.; Wang, C. Electrochemical stability of Li10GeP2S12 and $Li_7La_3Zr_2O_{12}$ solid electrolytes. *Adv. Energy Mater.* **2016**, *6*, 1501590.

(10) Lu, J.; Li, Y. Perovskite-type Li-ion solid electrolytes: a review. *J. Mater. Sci. Mater. Electron* **2021**, *32*, 9736−9754.

(11) Park, K.; Yu, B.-C.; Jung, J.-W.; Li, Y.; Zhou, W.; Gao, H.; Son, S.; Goodenough, J. B. Electrochemical nature of the cathode interface for a solid-state lithium-ion battery: interface between LiCoO2 and garnet-$Li_7La_3Zr_2O_{12}$. *Chem. Mater.* **2016**, *28*, 8051−8059.

(12) Kato, A.; Nose, M.; Yamamoto, M.; Sakuda, A.; Hayashi, A.; Tatsumisago, M. Mechanical properties of sulfide glasses in all-solid-state batteries. *J. Ceram. Soc. JAPAN* **2018**, *126*, 719−727.

(13) Yu, T.; Ke, B.; Li, H.; Guo, S.; Zhou, H. Recent advances in sulfide electrolytes toward high specific energy solid-state lithium batteries. *Mater. Chem. Front.* **2021**, *5*, 4892−4911.

(14) Richards, W. D.; Miara, L. J.; Wang, Y.; Kim, J. C.; Ceder, G. Interface stability in solid-state batteries. *Chem. Mater.* **2016**, *28*, 266−273.

(15) Ohta, N.; Takada, K.; Sakaguchi, I.; Zhang, L.; Ma, R.; Fukuda, K.; Osada, M.; Sasaki, T. LiNbO3-coated LiCoO2 as cathode material for all solid-state lithium secondary batteries. *Electrochem. commun.* **2007**, *9*, 1486−1490.

(16) Wang, C.; Liang, J.; Hwang, S.; Li, X.; Zhao, Y.; Adair, K.; Zhao, C.; Li, X.; Deng, S.; Lin, X.; et al. Unveiling the critical role of interfacial ionic conductivity in all-solid-state lithium batteries. *Nano Energy* **2020**, *72*, 104686.

(17) Asano, T.; Sakai, A.; Ouchi, S.; Sakaida, M.; Miyazaki, A.; Hasegawa, S. Solid Halide Electrolytes with High Lithium-Ion Conductivity for Application in 4 V Class Bulk-Type All-Solid-State Batteries. *Adv. Mater.* **2018**, *30*, 1803075.

(18) Park, K.-H.; Kaup, K.; Assoud, A.; Zhang, Q.; Wu, X.; Nazar, L. F. High-voltage superionic halide solid electrolytes for all-solid-state Li-ion batteries. *ACS Energy Lett.* **2020**, *5*, 533−539.

(19) Zhou, L.; Kwok, C. Y.; Shyamsunder, A.; Zhang, Q.; Wu, X.; Nazar, L. F. A new halospinel superionic conductor for high-voltage all solid state lithium batteries. *Energy Environ. Sci.* **2020**, *13*, 2056−2063.

(20) Kim, S. Y.; Kaup, K.; Park, K.-H.; Assoud, A.; Zhou, L.; Liu, J.; Wu, X.; Nazar, L. F. Lithium Ytterbium-Based Halide Solid Electrolytes for High Voltage All-Solid-State Batteries. *ACS Mater. Lett.* **2021**, *3*, 930−938.

(21) Zhou, L.; Zuo, T.-T.; Kwok, C. Y.; Kim, S. Y.; Assoud, A.; Zhang, Q.; Janek, J.; Nazar, L. F. High areal capacity, long cycle life 4 V ceramic all-solid-state Li-ion batteries enabled by chloride solid electrolytes. *Nat. Energy* **2022**, *7*, 83−93.

(22) Xu, X.; Huo, H.; Jian, J.; Wang, L.; Zhu, H.; Xu, S.; He, X.; Yin, G.; Du, C.; Sun, X. Radially oriented single-crystal primary nanosheets enable ultrahigh rate and cycling properties of LiNi0. 8Co0. 1Mn0. 1O2 cathode material for lithium-ion batteries. *Adv. Energy Mater.* **2019**, *9*, 1803963.

(23) Han, Y.; Jung, S. H.; Kwak, H.; Jun, S.; Kwak, H. H.; Lee, J. H.; Hong, S. T.; Jung, Y. S. Single-or Poly-Crystalline Ni-Rich Layered Cathode, Sulfide or Halide Solid Electrolyte: Which Will be the Winners for All-Solid-State Batteries? *Adv. Energy Mater.* **2021**, *11*, 2100126.

(24) Ryu, H.-H.; Park, K.-J.; Yoon, C. S.; Sun, Y.-K. Capacity fading of Ni-rich Li [Ni x Co y Mn1−x−y] O2 (0.6≤ x≤ 0.95) cathodes for high-energy-density lithium-ion batteries: bulk or surface degradation? *Chem. Mater.* **2018**, *30*, 1155−1163.
(25) Zhu, J.; Sharifi-Asl, S.; Garcia, J. C.; Iddir, H. H.; Croy, J. R.; Shahbazian-Yassar, R.; Chen, G. Atomic-Level Understanding of Surface Reconstruction Based on Li [Ni x Mn y Co1−x−y] O2 Single-Crystal Studies. *ACS Appl. Energy Mater.* **2020**, *3*, 4799−4811.
(26) Zhu, J.; Chen, G. Single-crystal based studies for correlating the properties and high-voltage performance of Li [Ni x Mn y Co 1− x− y] O 2 cathodes. *J. Mater. Chem. A* **2019**, *7*, 5463−5474.
(27) Liu, X.; Zheng, B.; Zhao, J.; Zhao, W.; Liang, Z.; Su, Y.; Xie, C.; Zhou, K.; Xiang, Y.; Zhu, J.; et al. Electrochemo-Mechanical Effects on Structural Integrity of Ni-Rich Cathodes with Different Microstructures in All Solid-State Batteries. *Adv. Energy Mater.* **2021**, *11*, 2003583.
(28) Ryu, H.-H.; Namkoong, B.; Kim, J.-H.; Belharouak, I.; Yoon, C. S.; Sun, Y.-K. Capacity fading mechanisms in Ni-rich single-crystal NCM cathodes. *ACS Energy Lett.* **2021**, *6*, 2726−2734.
(29) Zhang, F.; Lou, S.; Li, S.; Yu, Z.; Liu, Q.; Dai, A.; Cao, C.; Toney, M. F.; Ge, M.; Xiao, X.; et al. Surface regulation enables high stability of single-crystal lithium-ion cathodes at high voltage. *Nat. Commun.* **2020**, *11*, 1−11.
(30) Conforto, G.; Ruess, R.; Schröder, D.; Trevisanello, E.; Fantin, R.; Richter, F. H.; Janek, J. Editors' Choice—Quantification of the Impact of Chemo-Mechanical Degradation on the Performance and Cycling Stability of NCM-Based Cathodes in Solid-State Li-Ion Batteries. *J. Electrochem. Soc.* **2021**, *168*, 070546.
(31) Wang, C.; Yu, R.; Hwang, S.; Liang, J.; Li, X.; Zhao, C.; Sun, Y.; Wang, J.; Holmes, N.; Li, R.; et al. Single crystal cathodes enabling high-performance all-solid-state lithium-ion batteries. *Energy Storage Mater.* **2020**, *30*, 98−103.
(32) Payandeh, S.; Goonetilleke, D.; Bianchini, M.; Janek, J.; Brezesinski, T. Single versus poly-crystalline layered oxide cathode materials for solid-state battery applications-a short review article. *Curr. Opin Electrochem* **2022**, *31*, 100877.
(33) Zhang, Q.; Cao, D.; Ma, Y.; Natan, A.; Aurora, P.; Zhu, H. Sulfide-based solid-state electrolytes: synthesis, stability, and potential for all-solid-state batteries. *Adv. Mater.* **2019**, *31*, 1901131.
(34) Zhu, Y.; He, X.; Mo, Y. First principles study on electrochemical and chemical stability of solid electrolyte−electrode interfaces in all-solid-state Li-ion batteries. *J. Mater. Chem. A* **2016**, *4*, 3253−3266.
(35) Liu, X.; Shi, J.; Zheng, B.; Chen, Z.; Su, Y.; Zhang, M.; Xie, C.; Su, M.; Yang, Y. Constructing a high-energy and durable single-crystal NCM811 cathode for all-solid-state batteries by a surface engineering strategy. *ACS Appl. Mater. Interfaces* **2021**, *13*, 41669−41679.
(36) Schlem, R.; Muy, S.; Prinz, N.; Banik, A.; Shao-Horn, Y.; Zobel, M.; Zeier, W. G. Mechanochemical synthesis: a tool to tune cation site disorder and ionic transport properties of Li3MCl6 (M= Y, Er) superionic conductors. *Adv. Energy Mater.* **2020**, *10*, 1903719.
(37) Wang, S.; Zhang, X.; Liu, S.; Xin, C.; Xue, C.; Richter, F.; Li, L.; Fan, L.; Lin, Y.; Shen, Y.; et al. High-conductivity free-standing Li6PS5Cl/poly (vinylidene difluoride) composite solid electrolyte membranes for lithium-ion batteries. *J. Materiomics* **2020**, *6*, 70−76.
(38) Whiteley, J. M.; Taynton, P.; Zhang, W.; Lee, S. H. Ultra-thin solid-state Li-ion electrolyte membrane facilitated by a self-healing polymer matrix. *Adv. Mater.* **2015**, *27*, 6922−6927.
(39) Doux, J.-M.; Yang, Y.; Tan, D. H.; Nguyen, H.; Wu, E. A.; Wang, X.; Banerjee, A.; Meng, Y. S. Pressure effects on sulfide electrolytes for all solid-state batteries. *J. Mater. Chem. A* **2020**, *8*, 5049−5055.
(40) Ji, W.; Zheng, D.; Zhang, X.; Ding, T.; Qu, D. A kinetically stable anode interface for Li 3 YCl 6-based all-solid-state lithium batteries. *J. Mater. Chem. A* **2021**, *9*, 15012−15018.
(41) Luo, S.; Wang, Z.; Li, X.; Liu, X.; Wang, H.; Ma, W.; Zhang, L.; Zhu, L.; Zhang, X. Growth of lithium-indium dendrites in all-solid-state lithium-based batteries with sulfide electrolytes. *Nat. Commun.* **2021**, *12*, 1−10.
(42) Hänsel, C.; Singh, B.; Kiwic, D.; Canepa, P.; Kundu, D. Favorable Interfacial Chemomechanics Enables Stable Cycling of High-Li-Content Li−In/Sn Anodes in Sulfide Electrolyte-Based Solid-State Batteries. *Chem. Mater.* **2021**, *33*, 6029−6040.
(43) Santhosha, A.; Medenbach, L.; Buchheim, J. R.; Adelhelm, P. The indium− lithium electrode in solid-state lithium-ion batteries: phase formation, redox potentials, and interface stability. *Batter. Supercaps* **2019**, *2*, 524−529.
(44) Walther, F.; Randau, S.; Schneider, Y.; Sann, J.; Rohnke, M.; Richter, F. H.; Zeier, W. G.; Janek, J. r. Influence of carbon additives on the decomposition pathways in cathodes of lithium thiophosphate-based all-solid-state batteries. *Chem. Mater.* **2020**, *32*, 6123−6136.
(45) Zhang, W.; Leichtweiß, T.; Culver, S. P.; Koerver, R.; Das, D.; Weber, D. A.; Zeier, W. G.; Janek, J. r. The detrimental effects of carbon additives in Li10GeP2S12-based solid-state batteries. *ACS Appl. Mater.* **2017**, *9*, 35888−35896.
(46) Sun, H. H.; Ryu, H.-H.; Kim, U.-H.; Weeks, J. A.; Heller, A.; Sun, Y.-K.; Mullins, C. B. Beyond doping and coating: prospective strategies for stable high-capacity layered Ni-rich cathodes. *ACS Energy Lett.* **2020**, *5*, 1136−1146.
(47) Trevisanello, E.; Ruess, R.; Conforto, G.; Richter, F. H.; Janek, J. Polycrystalline and single crystalline NCM cathode materials—quantifying particle cracking, active surface area, and lithium diffusion. *Adv. Energy Mater.* **2021**, *11*, 2003400.
(48) Zhang, W.; Weber, D. A.; Weigand, H.; Arlt, T.; Manke, I.; Schröder, D.; Koerver, R.; Leichtweiss, T.; Hartmann, P.; Zeier, W. G.; et al. Interfacial processes and influence of composite cathode microstructure controlling the performance of all-solid-state lithium batteries. *ACS Appl. Mater. Interfaces* **2017**, *9*, 17835−17845.

https://doi.org/10.1021/acsenergylett.2c02414
ACS Energy Lett. 2023, 8, 521−528